Journal of The Electrochemical Society, **154** (12) A1077-A1082 (2007)
0013-4651/2007/154(12)/A1077/6/$20.00 © The Electrochemical Society

Electrochemical Behavior of Nanocrystalline $Ru_{0.8}Me_{0.2}O_{2-x}$ (Me = Fe, Co, Ni) Oxide Electrodes in Double-Layer Region

K. Macounová, I. Jirka, A. Trojánek, M. Makarova, Z. Samec,* and P. Krtil*,z

J. Heyrovsky Institute of Physical Chemistry of ASCR, Prague, Czech Republic

Nanocrystalline oxides with average chemical composition corresponding to $Ru_{0.8}Me_{0.2}O_{2-x}$ (Me = Fe, Co, Ni) were prepared by the sol-gel approach. All prepared materials were of single-phase character with rutile-type structure. The effect of nanocrystal size and nature of doping cation on electrochemical supercapacitor behavior was studied by means of cyclic voltammetry and electrochemical impedance. The specific capacitance of the Ru-based oxides increases by doping with lower-valence cation from ca. 22 $\mu F\ cm^{-2}$ of actual electrode surface area observed for pure RuO_2 to 230 $\mu F\ cm^{-2}$ in the case of Ni doped material. The improved capacitance behavior of the doped materials is ascribed to improvement of transport properties of the oxide structure enabling easier diffusion of compensating protons.
 [DOI: 10.1149/1.2783774]

Manuscript submitted March 30, 2007; revised manuscript received July 31, 2007. Available electronically September 28, 2007.

Transition metal oxides based supercapacitors represent an electrochemical power source surpassing the power density and life cycle of the current batteries.[1,2] The attainable energy density and stability of the metal oxide based supercapacitors are superior to those achieved for systems based on carbon materials or polymers.[3-5] The original concept of hydrous ruthenium dioxide electrodes[6] was later extended to other anhydrous materials of rutile,[7] perovskite,[8] or pyrochlore[9] structures with the aim to improve the utilization of the employed noble metal. The specific surface charge densities of the anhydrous oxides are reported to be, however, inferior to those of hydrous RuO_2.[6] The superior behavior of the hydrous oxides can be attributed to their structure, in which the micro/nanoislands of crystalline anhydrous oxide coexist with amorphous hydrous oxide. This coexistence increases significantly the mobility of the protons in the solid phase, which may be considered to be the rate limiting process.[10]

The main synthetic approach used in the rutile structural family to increase the noble metal utilization is the substitution of Ru or Ir in the cationic sublattice. From the synthetic point of view, substituted single-phase oxides with rutile structure may be prepared either by homovalent substitution (Ti [11], Zr [12], Ce [11,13], or Sn [11,14,15]) or by heterovalent substitution.[16-18] For both types of substitution, an increase in attainable specific surface charge was observed. The actual mechanism of this improvement and the role of the nature of the doping cation remains unknown.

This paper summarizes the capacitive behavior of several nanocrystalline doped Ru-based oxides conforming to the summary formula $Ru_{0.8}Me_{0.2}O_{2-x}$, where Me represents iron, cobalt, or nickel. The cyclic voltammetry and electrochemical impedance measurement data are related to the diffraction and microscopic characteristics of the electrode materials to describe the effects of the doping cation nature and nanocrystal size on the pseudocapacitive behavior of these materials.

Experimental

Nanocrystalline anhydrous RuO_2, and $Ru_{0.8}Me_{0.2}O_{2-x}$ (where Me stands for Co, Ni, or Fe) materials were prepared by a sol-gel synthesis analogue with that reported in Ref. 16. $Ru(NO)(NO_3)_3$ (Alfa Aesar) was dissolved in a 1:1 (v/v) mixture of 2-propanol and ethanol (both Aldrich, ACS grade) to obtain a starting solution with Ru concentration of 0.03 mol/L. In the case of $Ru_{1-x}Me_xO_{2-y}$ materials, the above starting solution was complemented by adding $Ni(NO_3)_2{\cdot}6H_2O$, $Co(NO_3)_2{\cdot}6H_2O$, and $Fe(NO_3)_2{\cdot}9H_2O$ (Lachema, p.a. grade), respectively, to obtain the solution with Ru:Me ratio of 4:1. The overall concentration of cations (i.e., of Ru and doping metal Me) remains the same as in the case of RuO_2 synthesis. Starting solutions were precipitated with aqueous solution (25 wt %) of tetramethylammonium hydroxide (TMAH) (Fluka). Resulting colloidal solution of an amorphous precursor was first aged in a polytetrafluethylene (PTFE)-lined stainless steel autoclave at 100°C for 40 h and then filtered. The amorphous precursor was then washed with deionized water (Millipore MilliQ quality) and with 1 mL of H_2O_2 solution (<1%) and subsequently recrystallized at temperatures between 400°C and 800°C to obtain nanocrystalline anhydrous oxides of various crystal size.

The crystallinity and phase purity of the prepared samples was checked using Bruker D8 Advanced powder X-ray diffractometer with Vantec-1 detector and Cu Kα radiation. Particle size distribution curves were obtained by analysis of scanning electron microscope (SEM) micrographs recorded employing Hitachi S4800 scanning electron microscope. The analysis was based on measurement of 150 randomly selected particles.

The chemical analysis of the surface of prepared samples was based on X-ray photoelectron spectroscopy (XPS). The photoelectron spectra of the $Ru_{0.8}Me_{0.2}O_{2-x}$ samples were measured using spectrometer ESC A 3 Mk II (VG) equipped with hemispherical analyzer in a fixed transmission mode. Photoelectrons were excited using nonmonochrornatized Al $K\alpha_{1,2}$ X-rays. Vacuum level maintained during experiments was better than 10^{-9} Torr. Samples were measured in the powder state using a double-sided Scotch tape. Surface concentration of Me was expressed in terms of Me/Ru atomic ratio calculated from the intensities of Ru 4p ($E_b \sim 45$ eV) and Co 3p ($E_b \sim 60$ eV), Ni 3p ($E_b \sim 68$ eV), Fe 3p ($E_b \sim 56$ eV), and normalized on the pertinent values of photoionization cross sections.[19] Binding energy E_b values were calibrated using E_b of C 1s photoelectron line (284.8 eV) of the adventitious carbon.

The electrochemical characterization of the prepared materials was performed in a single-compartment glass cell with RuO_2 or $RuO_{0.8}Me_{0.2}O_{2-x}$ based working electrode, saturated calomel reference electrode and Pt counter electrode. The reference electrode (containing KCl) was separated by a salt bridge filled with 0.1 M $NaNO_3$. The potential control was achieved using PAR 263A potentiostat. The electrochemical impedance spectroscopy measurements were carried out in the same three-electrode arrangement using Autolab P30 potentiostat in the frequency range from 50 kHz to 0.1 Hz with an ac amplitude of 10 mV (peak to peak). Impedance data were analyzed using Z-Plot/Z-View software (Scribner Associates). All experiments were carried out in 0.1 M $HClO_4$ (Aldrich p.a.). The $RuO_2/RuO_{0.8}Me_{0.2}O_{2-x}$ working electrodes were prepared on Ti mesh substrate (open area 20%, Goodfellow) by sedimentation of synthesized nanocrystalline powders from an aqueous suspension (5 g/L). The deposition of the oxides on the Ti substrate proceeded

* Electrochemical Society Active Member.
z E-mail: Petr.Krtil@jh-inst.cas.cz

Table I. Rietveld analysis-based lattice constants and mean particle size determined from SEM micrographs of nanocrystalline $Ru_{0.8}Me_{0.2}O_x$ materials.

Me	$t_{synthesis}$ (°C)	a (Å)	c (Å)	d (nm)
Fe	400	4.48	3.10	8.1
Co	400	4.48	3.08	20
Co	600	4.49	3.09	30
Co	800	4.50	3.10	60
Ni	400	4.48	3.10	66
Ni	600	4.49	3.10	106

in five steps to achieve the overall surface coverage in the range of 1–2 mg/cm^2. The oxide layer at the electrode was stabilized by drying at 100°C between individual depositions. The final deposition was followed by annealing the electrode at 400°C for 30 min.

Results and Discussion

Structural characterization.— As follows from the results of the XRD measurements, all prepared materials correspond to nanocrystalline single phases with tetragonal structure of rutile type (P_{42}/mnm). The temperature stability interval, however, differs for materials doped with different cations. Although the Co doped oxides retain the single phase character at temperatures below 800°C,[17] the Ni doped oxides decompose to RuO_2 and NiO at temperatures above 600°C; the materials doped with Fe form RuO_2 and hematite at temperatures exceeding 400°C. The lattice cell parameters provided by the Rietveld refinement of measured XRD data are summarized, along with the mean particle size values in Table I. As follows from the data shown in Table I, the doping of the ruthenium dioxide with Fe, Co, and Ni does not lead to significant modification of the unit cell parameters.[20] This is somewhat surprising, keeping in mind that all the used doping cations are stable in lower oxidation state(s) than that compatible with rutile structure (IV). Lowered overall charge in the cationic sublattice should lead to a relatively large number of point defects, which in turn should affect the unit cell parameters. This apparent disagreement can be explained, in part, assuming a nonhomogeneous distribution of doping cations within the nanocrystals, which was reported for Ru-Co-O phases, previously.[18] The confinement of doping cations (and point defects associated with them) into layers close to the surface would make them less affecting the bulk XRD patterns. The increase in applied calcination temperature leads to an improvement of the crystallinity, which manifests in increasing particle size[16] (see Fig. 1). It should be noted that the doping process affects the average particle size of the material. The nondoped RuO_2 materials feature, as a rule, finer particles compared to the doped oxides prepared at the same temperature. The only exclusion to this rule is the Fe doped oxide, which features crystals with an average size of 8 nm. The variability in characteristic particle size connected with the nature of doping cation (more than one order of magnitude) is particularly inconvenient if one attempts to compare the actual electrochemical activity of the oxides with different doping cations using mass related specific capacity (see Table II). The apparently higher utilization of the material with significantly finer particles does not necessarily reflect the true activity of the tested material; for this reason, the pseudocapacitance data are shown normalized to the actual physical area of the electrode materials.

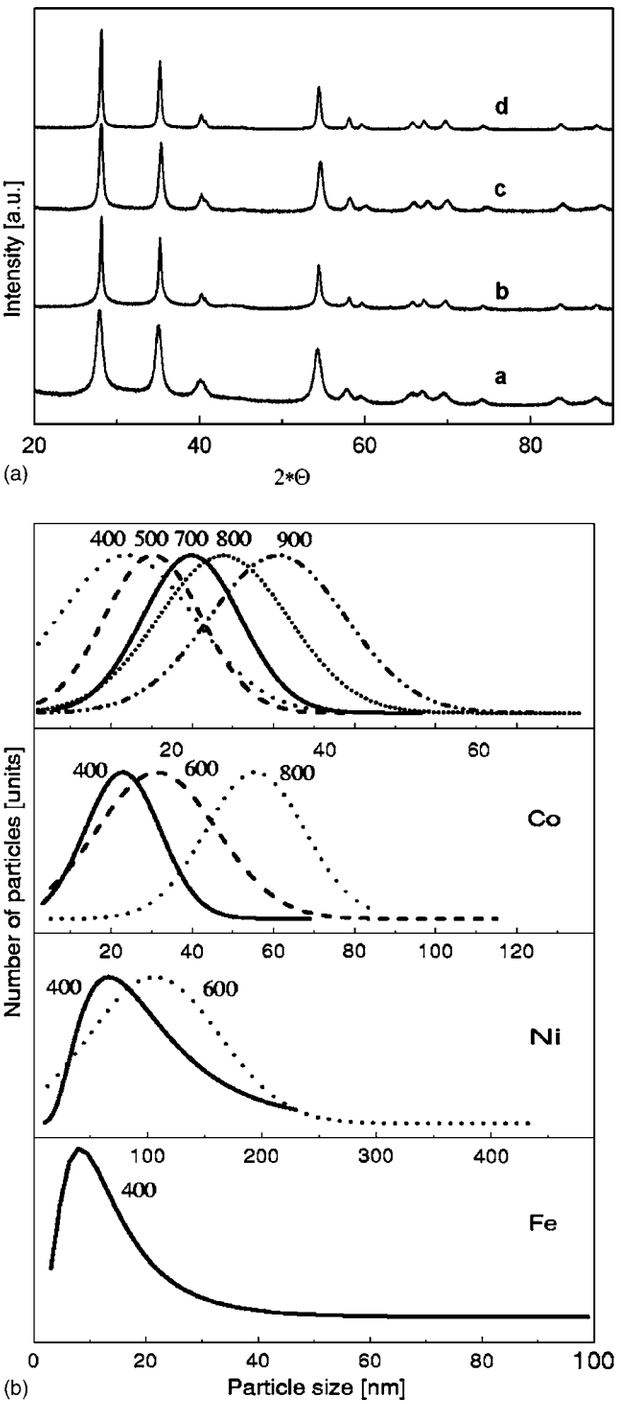

Figure 1. (a) Powder X-ray diffractograms of the nanocrystalline: a, RuO_2; b, $Ru_{0.8}Fe_{0.2}O_{2-x}$; c, $Ru_{0.8}Co_{0.2}O_{2-x}$; d, $Ru_{0.8}Ni_{0.2}O_{2-x}$. All samples were prepared at 400°C. (b) Particle size distributions for $Ru_{0.8}Me_{0.2}O_x$. The curve assignment is given in the figure legend.

Surface composition.— Although X-ray diffraction provides indirect information about chemical composition of the prepared materials, it is unable to provide information on the actual redox composition of the prepared materials or on possible nonhomogeneous distribution of the doping cation in the prepared materials. This drawback can be partially overcome by application of X-ray photolectron spectroscopy. The inherent surface sensitivity of the XPS approach along with the possibility to address the individual oxidation states makes this approach particularly suitable for characterization of the prepared materials. The results of the XPS spectroscopy measurements are summarized in Table III.

As show the data in Table III, the XPS technique indicates generally a nonhomogeneous distribution of the doping cation in the prepared nanocrystals. Whereas in the case of cobalt doped oxides, the actual ratio of both present cations approaches the projected average chemical composition, in the case of Ni and Fe doped ox-

Table II. Mass-related specific capacity for nanocrystalline RuO_2 and $Ru_{0.8}Me_{0.2}O_x$ materials.

Me	$t_{synthesis}$ (°C)	Specific surface area (m^2/g)	Mass specific capacity[a] ac (F/g)	Mass specific capacity[b] CV (F/g)
–	400	67.0	–	38.2
–	500	61.2	1	20.6
Fe	400	113.0	31.6	27.1
Co	400	42.6	29.7	39.2
Co	600	28.3	14.9	23.8
Co	800	14.1	11.4	12.5
Ni	400	14.0	13.9	21.6
Ni	600	8.7	8.3	12.5

[a] Values calculated on the basis of impedance spectroscopy.
[b] Values calculated on the basis of cyclic voltammetry.

ides, the surface layer of the doped oxide is significantly enriched with the doping cation with respect to the projected average chemical composition. Although, in the case of Ni doped materials, the ruthenium still remains the major transition metal in the near surface layer, the Fe doped oxides feature the iron as the principal transition metal cation in the near surface layer showing twice higher iron content than that of ruthenium. The oxygen content in the near surface layer increases with increasing amount of the doping cation.

The trend in chemical composition shown in Table III is difficult to rationalize. Regardless of the nature, the doping cations show typically a lower valency in their compound than IV. Reflecting the fact that the doping most likely leads to a lowered charge in the cationic sublattice of the prepared oxide, one can propose two different mechanisms of charge compensation. One can either expect a presence of oxygen vacancies or stabilization of Ru in oxidation state higher than IV within the material structure.[17] As follows from the XPS measurement, the former mechanism is more likely in the case of material doped with cobalt, whereas the Ni and Fe doped oxides are more likely to adopt the later mechanism (see Table III). The XPS data do not allow, however, for a direct determination of the oxidation state distribution mainly because of the overlap of the Ru 3d and C 1s lines, which prevents correct analysis of the Ru spectral line. Additional X-ray absorption experiments would be needed to resolve the issue of the oxidation states distribution conclusively.

Voltammetric behavior.— Typical cyclic voltammograms of the prepared RuO_2 and $Ru_{0.8}Me_{0.2}O_{2-x}$ electrodes in the double-layer region are shown in Fig. 2. The cyclic voltammograms observed for undoped RuO_2 resemble those reported previously.[21] In the case of doped materials, one does not observe any resolved signal attributable to any surface well-defined redox process except for the broad peak at ca. 500 mV, which is complemented by a cathodic signal at ca. 420 mV. It is rather difficult, in contrast to undoped RuO_2 material, to assign this peak to any definite redox process, because one

Table III. Chemical composition of the surface of prepared materials calculated on the basis of XPS spectra.

Me	$t_{synthesis}$ (°C)	Me:Ru	O:Ru
–	400	–	1.2
Fe	400	1.42	5.35
Co	400	0.23	2.17
Co	600	0.27	2.28
Co	800	0.32	3.41
Ni	400	0.75	4.88
Ni	600	0.74	5.11

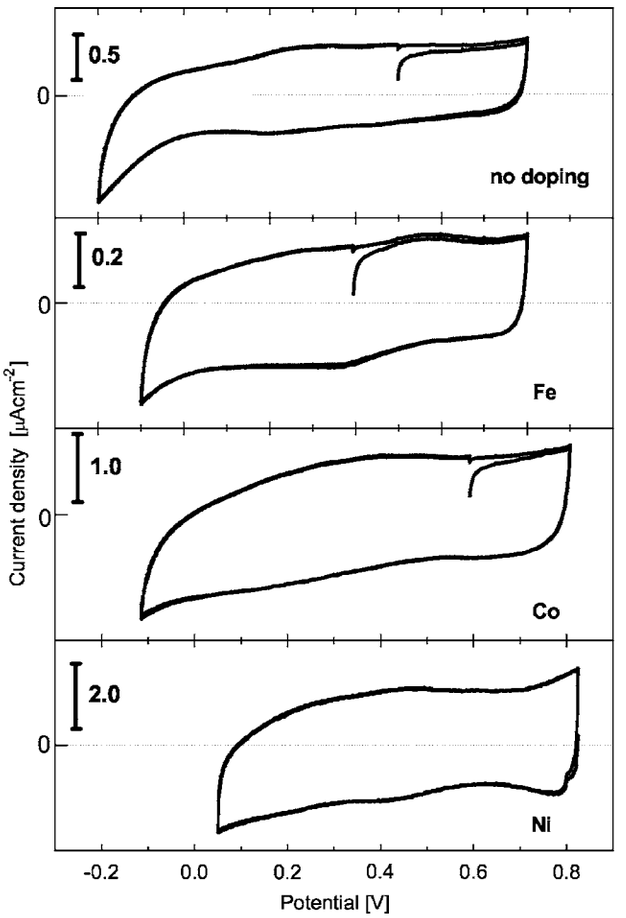

Figure 2. The effect of the doping on the voltammetric behavior of $Ru_{0.8}Me_{0.2}O_x$-based nanostructured electrodes in the double-layer region in 0.1 M $HClO_4$. The applied scan rate was 10 mV/s. All samples were prepared at 400°C. The curve assignment is given in the legend. The presented current densities are related to the actual electrode surface area calculated from average particle size, assuming spherical shape of the particles.

has to be aware of the fact that not only Ru but also the doping cation may be involved in redox processes. The charge obtained by integration of the measured current over the entire applied potential interval, which is directly related to applicability of the studied oxides in supercapacitors, shows pronounced dependence on the applied experimental time scale for all studied materials, indicating the pseudocapacitance character of the charge storage (see Fig. 3). The analysis of all experimental data on the charge, which can be stored per unit area of the actual surface of different materials with rutile structure, shows two general trends (see Fig. 3). First, in the case of RuO_2 samples, the storable charge increases with decreasing particle size (see Fig. 3a). Second, in the case of doped materials, the effect of actual particle size on the storable charge is less pronounced, probably due to the effect of the doping cation presence. The materials doped with cobalt or nickel always show higher storable charge than undoped RuO_2 materials, regardless of the actual particle size (see Fig. 3b). The storable charge observed for Fe doped materials is smaller than that of RuO_2 of the same particle size.

Although the effect of the particle size dependence observed for differently sized RuO_2 nanocrystals is difficult to rationalize without employment of surface sensitive techniques, such as XPS, the effect of the doping cation may be addressed using an approach similar to that commonly used in Li insertion electrochemistry.

One may reasonably expect that the charge recorded during cycling the Ru-based oxide electrodes in the double layer region in

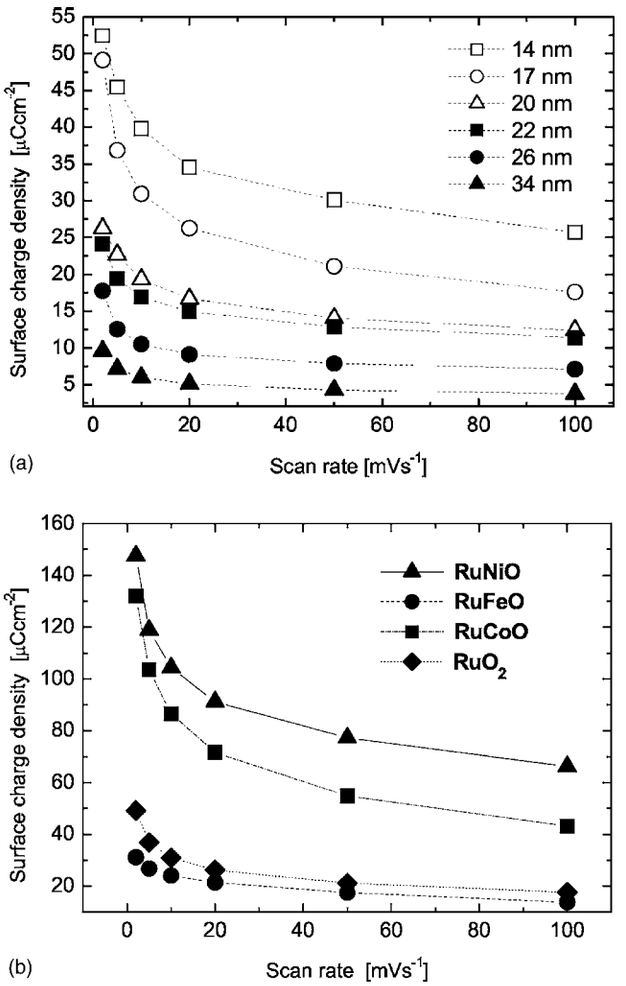

Figure 3. (a) Surface charge density of nanocrystalline RuO_2 and (b) doped $Ru_{0.8}Me_{0.2}O_{2-x}$-based nanostructured electrodes as a function of applied scan rate. All samples in (b) were prepared at 400°C. The symbol assignment is given in the legend.

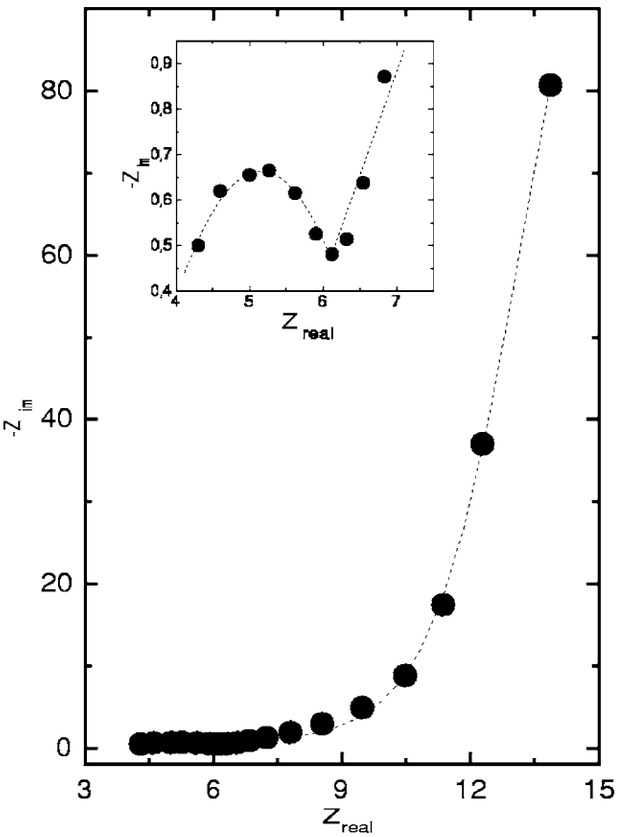

Figure 4. Typical impedance spectrum of $Ru_{0.8}Co_{0.2}O_{2-x}$ electrode polarized at 600 mV. Inset shows a zoom of the high-frequency arc.

fact corresponds to an oxidation/reduction of the electrode material, which is compensated, in part, by insertion/extraction of a cation (proton) into/from the electrode structure.[22] As follows from theoretical analysis of the insertion systems, the attainable capacity can be affected either by structure of the electrode material or by the kinetics of the insertion process. It ought to be noted that the electrode material structure affects the attainable capacity in two ways; by variation of the concentration of oxidizable/reducible metal ions and by availability of vacant sites needed for compensating cations. Keeping in mind that the storable charge recorded during voltammetric experiments is by more than two orders of magnitude smaller than what would correspond to complete a one electron reduction of all available Ru, we may disregard the alteration of the total concentration of the oxidizable/reducible metal ions resulting from material doping as the reason for the variation in storable charge. The kinetic effects affecting the pseudocapacitive behavior of doped oxides are most likely connected with a possible difference in transport properties of the material resulting from doping. All relevant characteristics describing both possible types of effects can be extracted from impedance behavior of the electrodes at different potentials. An example of typical impedance behavior of $Ru_{0.8}Co_{0.2-x}$ electrode is shown at Fig. 4.

Keeping in mind the similarity of the pseudocapacitive behavior with the ion insertion processes, one can use one of the equivalent circuits derived originally for the Li insertion systems to approximate the behavior of the studied electrode (see Fig. 5).[23] This predicts the response of the studied electrode to be composed of the contribution from uncompensated resistance (R1) of the system, a Randles-like component corresponding to electron transfer reaction (most likely Ru species oxidation/reduction) in series with a finite length Warburg element (W1) characterizing the transport of the compensation proton in the structure and a capacitance element CPE(1). The nonlinear least square (NLLS) fit of the impedance data at different potentials provides data related to important parameters, the capacitance and Warburg impedance (see Fig. 6 and 7, respectively).

The capacitance of all measured electrodes shows pronounced dependence on applied potential. The capacitance values are practically constant for potentials negative to 600 mV and start to increase exponentially at more positive potentials. Such a behavior was already observed for RuO_2 single crystal.[24] This increase is in accordance with expected proton insertion mechanism of the pseudocapacitive behavior of Ru-based oxides in acid media and reflects most likely an increase in the average oxidation state of Ru near the surface at these potentials.

The surface-related specific capacitance of the doped materials is higher than that of undoped materials. This can be intuitively attributed to the changes in the overall redox composition caused by the

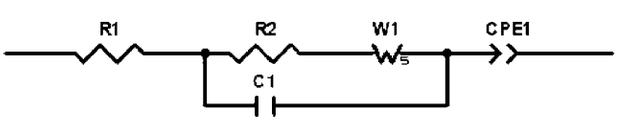

Figure 5. Equivalent circuit used in NLLS fit of the ac impedance data.

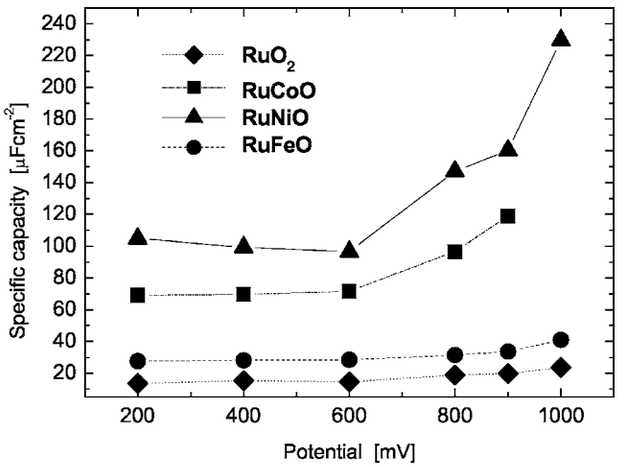

Figure 6. Electrochemical impedance-based differential capacitance as a function of electrode potential for nanostructured RuO_2 and $Ru_{0.8}Me_{0.2}O_{2-x}$ electrodes. All samples were prepared at 400°C. The symbol assignment is given in the legend. Original capacitance data were recalculated to actual electrode area based on average particle size, assuming spherical shape of the particles.

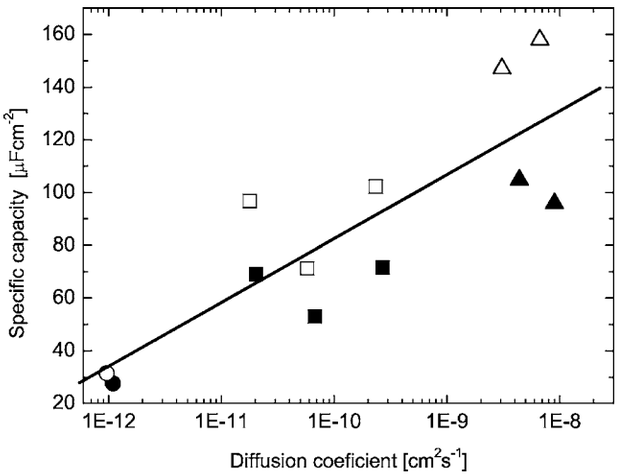

Figure 8. Differential capacitance of the nanostructured $Ru_{0.8}Me_{0.2}O_{2-x}$ electrodes as function of the proton diffusion coefficient. Me represents Co (■), Ni (▲) and Fe (●). The respective open symbols represent data measured at 200 mV; the solid symbols show data measured at 800 mV.

doping process. Comparing the effect of the nature of the doping cation, one finds that the specific capacitance increases in the order Fe < Co < Ni. It should be noted that specific capacitance in all studied ternary systems, i.e., Ru–Co–O, Ru–Fe–O, and Ru–Ni–O, is unaffected by the variation in particle size. The rationalization of the observed variation of the capacitance with the chemical nature of the doping cation is not straightforward. The observed capacitance values do not correlate with the surface fraction of Ru; one cannot assign the changes in observed capacitance values to suggested changes in redox composition of the prepared oxides since the charge corresponding to the measured capacitance is in all cases significantly smaller than that which may be attributed to a complete reduction/oxidation of the Ru present in the surface layer, theoretically.

Alternatively, one may attribute the increase of the specific capacitance to variations of materials transport phenomena, which can make the compensating protons more mobile in the oxide structure.

Complementary information needed for comparison of transport properties can be extracted from finite-length Warburg element,

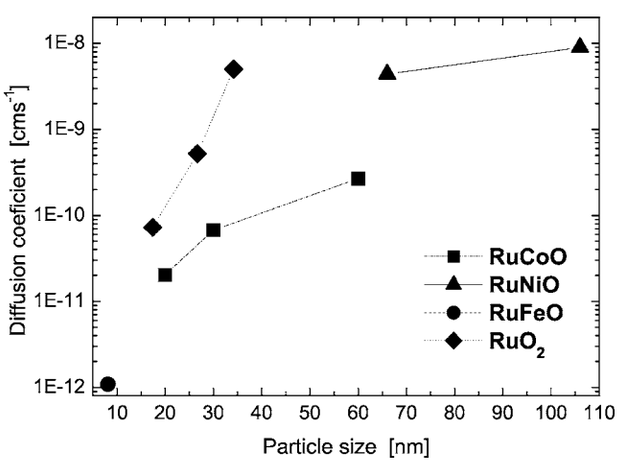

Figure 7. Nanocrystal size dependence of the proton diffusion coefficient for nanostructured RuO_2 and $Ru_{0.8}Me_{0.2}O_{2-x}$ electrodes. The symbol assignment is given in the legend.

which characterizes transport properties of the prepared materials. The characteristic time constant obtained from the Warburg impedance fit term can be related to characteristic particle size L and diffusion coefficient D[25]

$$T = \frac{L^2}{D}$$

The diffusion coefficients of all measured materials show negligible dependence on electrode potential. This behavior is not surprising, keeping in mind that the storable charge represents only a small fraction of the total bulk redox capacity of material; hence, we can anticipate only negligible changes in the occupancy of the lattice vacant positions, which is controlling the transport properties of the structure. The diffusion coefficient in all cases increases with increasing particle size. This trend is more pronounced for pure RuO_2 than for the doped materials. In the case of doped materials, this tendency seems to be more important for Co doped oxide than for Ni doped materials. Comparing absolute values of the proton diffusion coefficient shown in Fig. 7, one arrives to a conclusion that proton's mobility decreases going from Ru–Ni–O system to pure RuO_2, Ru–Co–O system and finally to the Ru–Fe–O system. The observed values of diffusion coefficient range between 10^{-8} cm^2 s^{-1} (in the case of Ru–Ni–O) and 10^{-12} cm^2 s^{-1} in the case of Ru–Fe–O. The fact that the RuO_2 materials with large particles exhibit comparable diffusion coefficient as the Ru–Ni–O oxide (which show by more than one order of magnitude higher specific capacitance) indicates that transport properties play a secondary role to overall redox composition in affecting the storable charge and specific capacitance. Transport properties do play an important role in explaining the differences in the specific capacitance of materials doped with different cations (see Fig. 8). The linear dependence of the specific capacitance on the diffusion coefficient observed for all doped oxides (regardless of the type of the doping cation) shows that the transport properties do suppress the actual changes in the redox composition.[18] The actual order of diffusion coefficients observed at materials doped with Ni, Co, and Fe may be explained by actual distribution of the doping cation within the oxide particles. Such a hypothesis would need to be confirmed, however, by an advanced structural study.

Conclusion

Nanocrystalline materials with an average composition of $Ruo_{0.8}Me_{0.2}O_{2-x}$ (Me stands for Fe, Co, and Ni) prepared by a sol-

gel approach are suitable for use in supercapacitors. The doped materials show superior capacitive behavior compared to that of pure RuO_2 prepared by the same synthetic approach. In contrast to undoped RuO_2 show negligible variability of the pseudocapacitive behavior on the actual particle size. The specific capacitance of all studied materials increases with increasing potential. This can be related to increasing average oxidation state of Ru in the nanocrystalline materials. The same mechanism is also proposed to explain the increasing specific capacitance of doped oxides. At doped oxide, the observed specific capacitance can be connected with an increase of the proton diffusion in the structure of doped materials, which decreases from 10^{-8} cm^2 s^{-1} in the case of Ru–Ni–O system to 10^{-12} cm^2 s^{-1} in the Ru–Fe–O system.

Acknowledgment

This work was supported by the Academy of Sciences of the Czech Republic under contract no. ET4004004013.

Academy of Sciences of the Czech Republic assisted in meeting the publication costs of this article.

References

1. B. E. Conway, *Electrochemical Supercapacitors*, Kluwer, Dordrecht (1999).
2. *Electrochemistry of Semiconductors and Electronics*, I. E. Raistrick, J. McHardy, and F. Ludwig, Editors, p. 297, Noyes, Park Ridge, NJ (1992).
3. S. Trassati, *Electrochim. Acta*, **36**, 225 (1991).
4. B. E. Conway, V. Birss, and J. Wojtowicz, *J. Power Sources*, **66**, 1 (1997).
5. Y. Takasu and Y. Murakami, *Electrochim. Acta*, **45**, 4135 (2000).
6. J. P. Zheng, P. G. Cyang, and T. R. Jow, *J. Electrochem. Soc.*, **142**, 2699 (1995).
7. W. Sugimoto, T. Shibutani, Y. Murakami, and Y. Takasu, *Electrochem. Solid-State Lett.*, **5**, A170 (2002).
8. P. M. Wilde, T. J. Guther, R. Oesten, and J. Garche, *J. Electroanal. Chem.*, **461**, 154 (1999).
9. F. Cao and J. Prakash, *J. Power Sources*, **92**, 40 (2001).
10. W. Dmowski, T. Egami, K. E. Swider-Lyons, C. T. Love, and D. R. Rolinson, *J. Phys. Chem. B*, **106**, 12677 (2002).
11. L. A. da Silva, V. A. Alves, M. A. P. da Silva, S. Trasatti, and J. F. C. Boodts, *Can. J. Chem.*, **75**, 1483 (1997).
12. O. R. Camara and S. Trasatti, *Electrochim. Acta*, **41**, 419 (1996).
13. L. A. DeFaria, J. F. C. Boodts, and S. Trasatti, *Electrochim. Acta*, **37**, 2511 (1992).
14. C. P. DePauli and S. Trasatti, *J. Electroanal. Chem.*, **538**, 145 (2002).
15. J. Gaudet, A. C. Tavares, S. Trasatti, and D. Guay, *Chem. Mater.*, **17**, 1570 (2005).
16. J. Jirkovsky, M. Makarova, and P. Krtil, *Electrochem. Commun.*, **8**, 1417 (2006).
17. S. Aridizzone, C. L. Bianchi, G. Cappelletti, M. Ionita, A. Minguzzi, S. Rondinini, and A. Vertova, *J. Electroanal. Chem.*, **589**, 160 (2006).
18. M. Makarova, J. Jirkovsky, M. Klementova, I. Jirka, K. Macounova, and P. Krtil, *Electrochim. Acta*, (2007).
19. J. Scofield, *J. Electron Spectrosc. Relat. Phenom.*, **8**, 129 (1976).
20. C. E. Boman, *Acta Chem. Scand. (1947-1973)*, **24**, 116 (1970).
21. T. Arikado, C. Iwakura, and H. Tamura, *Electrochim. Acta*, **22**, 513 (1977).
22. I.-H. Kim and K.-B. Kim, *J. Electrochem. Soc.*, **151**, E7 (2004).
23. M. D. Levi and D. Aurbach, *Electrochim. Acta*, **45**, 167 (1999).
24. M. Tomkiewicz, Y. S. Huang, and F. H. Pollak, *J. Electrochem. Soc.*, **130**, 1514 (1983).
25. J. Rishpon and S. Gottesfeld, *J. Electrochem. Soc.*, **131**, 1960 (1984).